Simple method for optimization of classical electron magnetic circular dichroism measurements: The role of structure factor and extinction distances

Sebastian Schneider,[1,2] Devendra Negi,[3] Matthew J. Stolt,[4] Song Jin,[4] Jakob Spiegelberg,[3] Darius Pohl,[5,1] Bernd Rellinghaus,[5,1] Sebastian T. B. Goennenwein,[2,6] Kornelius Nielsch,[1,7] and Ján Rusz[3,1,*]

[1]*Institute for Metallic Materials, IFW Dresden, Helmholtzstraße 20, 01069 Dresden, Germany*
[2]*Institut für Festkörper- und Materialphysik, Technische Universität Dresden, 01062 Dresden, Germany*
[3]*Department of Physics and Astronomy, Uppsala University, P.O. Box 516, 75120 Uppsala, Sweden*
[4]*Department of Chemistry, University of Wisconsin-Madison, 1101 University Avenue, Madison, Wisconsin 53706, USA*
[5]*Dresden Center for Nanoanalysis, Technische Universität Dresden, 01062 Dresden, Germany*
[6]*Center for Transport and Devices of Emergent Materials, Technische Universität Dresden, 01062 Dresden, Germany*
[7]*Institute of Materials Science, Technische Universität Dresden, Helmholtzstraße 7, 01069 Dresden, Germany*

(Received 13 June 2018; published 9 November 2018)

Electron magnetic circular dichroism (EMCD), the electron wave analog of x-ray magnetic circular dichroism (XMCD), allows for the element specific measurement of the spin and orbital magnetic moments with up to nanometer resolution. However, due to dynamical diffraction effects, the signal-to-noise ratios of EMCD spectra are often very low. We describe a simple set of rules, how to set up a geometry for a classical EMCD experiment on an arbitrary crystal structure to get a maximum dichroic signal. The procedure is based on an evaluation of the structure factor and extinction distances. Proof-of-concept simulations and experiments on a FeGe crystal present a successful test of these guidelines.

DOI: 10.1103/PhysRevMaterials.2.113801

I. INTRODUCTION

Electron magnetic circular dichroism (EMCD; [1]) is an experimental technique promising high spatial resolution quantitative magnetic measurements. Despite being in development for more than a decade, it hasn't yet reached widespread employment. The most likely reason for it is the complexity of dynamical diffraction effects. In consequence, the amplitude of the EMCD spectrum is often very low, obfuscated by noise. It becomes necessary to optimize the experimental settings by performing inelastic-scattering calculations in various experimental geometries, which is a routine, though complex, task for a theorist.

Omitting the subtopic of atomic resolution EMCD experiments, where one utilizes highly convergent electron beams [2–4], the most common geometries for so-called *classical* EMCD experiments involve orienting the crystal into a systematic row condition indexed by a chosen Bragg reflection **G**. This is typically achieved by tilting the sample 5–20° away from some high-symmetry orientation, zone axis (hkl). The tilt is within a plane parallel to (hkl) and perpendicular to **G**.

The originally proposed experimental geometry [1,5] was a two-beam orientation, in which the incoming parallel beam is tilted further so that an excitation error of a selected Bragg reflection (not necessarily equal to **G**) is zero. In this crystal orientation, the EMCD signal is expected to be seen mostly in the area between **0** and **G**, having opposite signs above and under the systematic row, respectively. It is extracted using

$$\mathrm{EMCD} \propto \sigma_{++}(E) - \sigma_{+-}(E),$$

where $\sigma_{++}(E)$ and $\sigma_{+-}(E)$ denote double-differential scattering cross sections integrated over a specific range of scattering angles; see Fig. 1(c). In the further text, explicit marking of energy dependence of σ will be omitted.

Another alternative is a three-beam geometry [6–8], where the excitation errors of $+\mathbf{G}$ and $-\mathbf{G}$ are kept equal. In this orientation, the EMCD signal is nonzero in all four quadrants of the diffraction plane, having alternating signs for all neighboring quadrants. An often quoted advantage of the three-beam orientation is its higher tolerance to asymmetries thanks to the so-called *double difference* procedure [7]:

$$\mathrm{EMCD} \propto (\sigma_{++} - \sigma_{+-}) - (\sigma_{-+} - \sigma_{--});$$

see Fig. 1(b).

It is important to note that the exact EMCD distribution in the diffraction plane still depends on several factors, most importantly on the crystal structure and sample thickness. Other factors are magnetic structure, acceleration voltage, and convergence angle of the beam. It is quite possible that even if one carefully and precisely orients the crystal into one of these two experimental geometries, the observed EMCD signal will be too low to be seen above the noise level. At this point, if the experiments were not successful, it is common to address the question of suitable experimental geometry by explicit simulation of the energy-filtered diffraction patterns [9–11], to find the optimal orientation, sample thickness, and detector orientation that would lead to the strongest EMCD signal.

In this paper we propose a simple procedure that should help to circumvent this step and equip an experimentalist with a simple set of rules on how to determine the optimal experimental geometry for classical EMCD experiments.

*jan.rusz@physics.uu.se

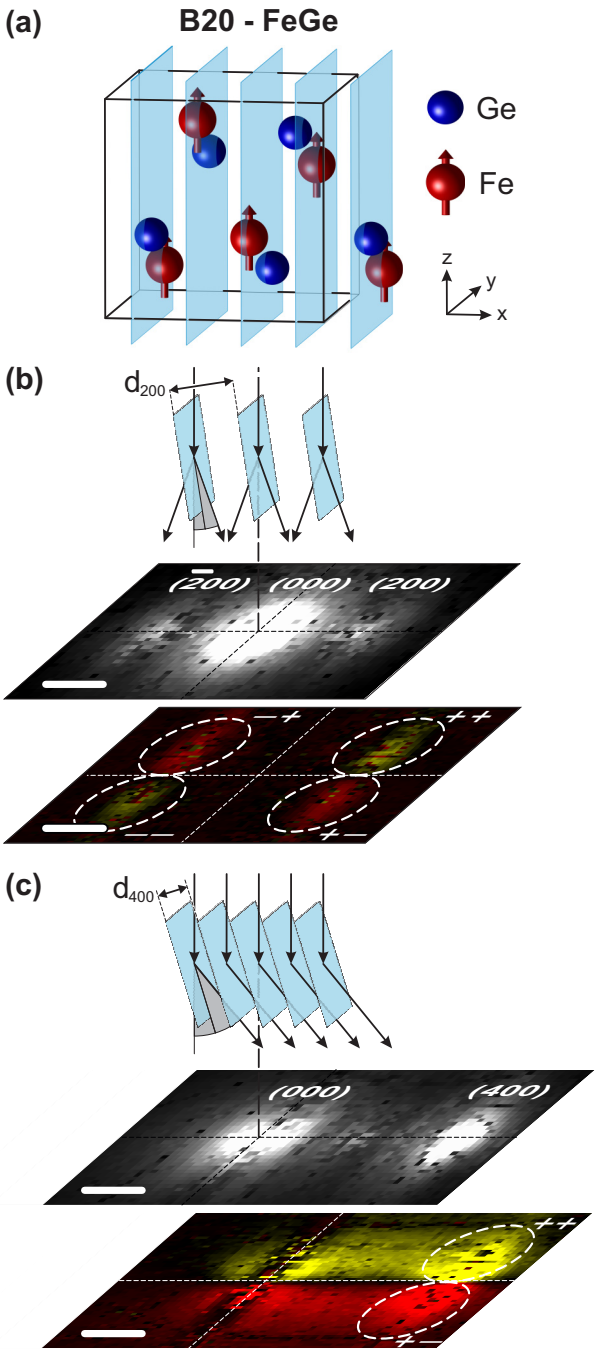

FIG. 1. (a) Crystallographic unit cell of stoichiometric FeGe in the B20 structure. The blue sheets indicate the {200} and {400} lattice planes, while the blue and red arrowed spheres represent the nonmagnetic Ge and the magnetic Fe atoms, respectively. Schematic illustration of the Bragg scattering of 300-keV electrons, which impinge on a B20 FeGe crystal under (b) (−200)(000)(200) three-beam orientation and (c) (000)(400) two-beam condition. Both the calculated diffraction patterns (upper grey scale maps) and EMCD maps (lower, colored maps) are shown for each of these cases. The scale bars refer to diffraction angles of 5 mrad. The distinct differences in the EMCD maps are attributed to the largely different *partial structure factors*. Dashed circles indicate the optimal positions of the entrance aperture of the EEL spectrometer in order to obtain maximum dichroic (EMCD) signals (see text for details and labeling).

Section II summarizes the role of the structure factor and how to use it to guide selection of suitable systematic row conditions. The role of the extinction distance will also be discussed in the context of thickness dependence of EMCD. In Sec. III we apply the optimization procedure to the example of a FeGe crystal and perform explicit simulations of inelastic-scattering cross section including double-channeling effects. In Sec. IV we show experimental results for the FeGe crystal, benefiting from the procedure described here. Section V discusses the findings and their extensions for more complicated magnetic structures.

II. STRUCTURE FACTOR

In a two-beam orientation with a strongly excited Bragg spot **G**, one can approximately write the electron-beam wave function in the following form:

$$\psi_{\text{in}}(\mathbf{r}) \approx C_{\mathbf{0}}(z)e^{i\mathbf{k}_{\text{in}}\cdot\mathbf{r}} + C_{\mathbf{G}}(z)e^{i(\mathbf{k}_{\text{in}}+\mathbf{G})\cdot\mathbf{r}}, \tag{1}$$

where the coefficients $C_{\mathbf{0}}(z), C_{\mathbf{G}}(z)$ can be expressed in a Bloch-waves picture as

$$C_{\mathbf{G}}(z) = \sum_j C_{\mathbf{0}}^{\star(j)} C_{\mathbf{G}}^{(j)} e^{i\gamma^{(j)}z}. \tag{2}$$

In these expressions, $C_{\mathbf{G}}^{(j)}$ is a Bloch-wave coefficient corresponding to beam **G** and Bloch wave j; the $\gamma^{(j)}$ is an elongation of the incoming wave vector (*Anpassung*) assuming sample surface normals are parallel to the z direction. Equation (1) neglects all the other beams for **H** different from **0** or **G**.

The inelastic-scattering cross section can be obtained by the first Born approximation, meaning that we assume only one inelastic-scattering event to occur during the passage of the beam through the sample. Considering that the inelastic-scattering mean free paths are on the order of 100 nm and sample thicknesses are typically 20–30 nm, the first Born approximation should offer a sufficient precision. As the final state in the first Born approximation, we need a wave function of the electron beam entering the detector. Here we adopt the simplest approximation for such a situation, describing such outgoing beam by a simple plane wave:

$$\psi_{\text{out}}(\mathbf{r}) \approx e^{i\mathbf{k}_{\text{out}}\cdot\mathbf{r}}, \tag{3}$$

where $\mathbf{k}_{\text{out}}$ is fixed by the detector orientation. Then the first Born approximation of inelastic scattering cross section can be written as

$$\frac{\partial^2\sigma}{\partial\Omega\partial E} = \frac{k_{\text{out}}}{k_{\text{in}}} \sum_{I,F} \left| \frac{m_e}{2\pi\hbar^2} \langle\psi_{\text{out}}| \otimes \langle F|\hat{V}|I\rangle \otimes |\psi_{\text{in}}\rangle \right|^2 \times \delta(E + E_I - E_F), \tag{4}$$

where m_e is the relativistic electron mass and I, F label initial and final (excited) states of the crystal, having energies E_I, E_F, respectively. The E represents the energy loss, i.e., the energy that the beam electron transfers to the sample in the excitation process, and $\hat{V}$ is Coulomb interaction operator representing interactions among all charges in the system (beam and sample).

For core-level excitations, which are the focus of our paper, the initial states I label all atoms, where the chosen excitation

can occur. We will label their positions with vectors **a**. For example, if we aim to measure EMCD on Fe L_3 edge in a FeGe crystal, then initial I labels ground states of all iron atoms. Final states, F, then represent all the excited states of the crystal, for which the $E_F - E_I$ is within a desired range of energy losses.

Inserting the explicit expressions for the $\psi_{\text{in}}, \psi_{\text{out}}$ one obtains for the two-beam orientation

$$\frac{\partial^2\sigma}{\partial\Omega\partial E} \propto \sum_{\mathbf{a}}[|C_{\mathbf{0}}(a_z)|^2 S_{\mathbf{a}}(\mathbf{Q},\mathbf{Q},E) + |C_{\mathbf{G}}(a_z)|^2 S_{\mathbf{a}}(\mathbf{Q}-\mathbf{G},\mathbf{Q}-\mathbf{G},E) + 2\text{Re}[e^{-i\mathbf{G}\cdot\mathbf{a}} C_{\mathbf{0}}(a_z) C^{\star}_{\mathbf{G}}(a_z) S_{\mathbf{a}}(\mathbf{Q},\mathbf{Q}-\mathbf{G},E)]], \quad (5)$$

where $\mathbf{Q} = \mathbf{k}_{\text{out}} - \mathbf{k}_{\text{in}}$ and

$$S_{\mathbf{a}}(\mathbf{q},\mathbf{q}',E) = \sum_F \langle I_{\mathbf{a}}| \frac{e^{i\mathbf{q}'\cdot(\mathbf{r}-\mathbf{a})}}{q'^2} |F\rangle\langle F| \frac{e^{-i\mathbf{q}\cdot(\mathbf{r}-\mathbf{a})}}{q^2} |I_{\mathbf{a}}\rangle \times \delta(E + E_I - E_F) \quad (6)$$

is a mixed dynamic form factor [12] (MDFF) of atom **a** expressed in its local coordinate system (centered around atom **a**).

The EMCD signal is contained in the imaginary part of the MDFF, which is zero if its first two arguments are equal, therefore only the last term of Eq. (5) can contribute with EMCD:

$$\text{EMCD} \propto -2\sum_{\mathbf{a}}[\text{Im}[e^{-i\mathbf{G}\cdot\mathbf{a}} C_{\mathbf{0}}(a_z) C^{\star}_{\mathbf{G}}(a_z)] \times \text{Im}[S_{\mathbf{a}}(\mathbf{Q},\mathbf{Q}-\mathbf{G},E)]]. \quad (7)$$

Assuming for simplicity that all atoms **a** are symmetrically equivalent and magnetically saturated in the external magnetic field of the microscope objective lens, the imaginary part of MDFF becomes **a** independent and can be taken outside of the summation. (See Sec. V below for a discussion of more general situations.) Therefore, if we want to optimize the absolute strength of EMCD, we need to maximize the magnitude of the following term:

$$\sum_{\mathbf{a}} \text{Im}[e^{-i\mathbf{G}\cdot\mathbf{a}} C_{\mathbf{0}}(a_z) C^{\star}_{\mathbf{G}}(a_z)]. \quad (8)$$

In a two-beam approximation for an exact two-beam orientation (i.e., with zero excitation error $s_{\mathbf{G}}$), there are only two Bloch waves, which can be obtained by secular equation [13],

$$\begin{pmatrix} -2K_z\gamma & U_{-\mathbf{G}} \\ U_{\mathbf{G}} & -2K_z\gamma \end{pmatrix} \begin{pmatrix} C_{\mathbf{0}} \\ C_{\mathbf{G}} \end{pmatrix} = 0, \quad (9)$$

where K_z is here the z component of the incoming beam wave vector $\mathbf{k}_{\text{in}}$ and $U_{\mathbf{G}} = \frac{2me}{\hbar^2} V_{\mathbf{G}}$, where $V_{\mathbf{G}}$ is a Fourier component of the electrostatic potential inside the sample. In general, for a noncentrosymmetric system $U_{-\mathbf{G}} = U^{\star}_{\mathbf{G}}$ and the solution is

$$C^{(1,2)}_{\mathbf{0}} = \frac{1}{\sqrt{2}} \quad \text{and} \quad C^{(1,2)}_{\mathbf{G}} = \pm\frac{e^{i\phi_{\mathbf{G}}}}{\sqrt{2}}, \quad (10)$$

$$\text{where} \quad U_{\mathbf{G}} = e^{i\phi_{\mathbf{G}}}|U_{\mathbf{G}}|, \quad (11)$$

$$\gamma^{(1,2)} = \pm\frac{|U_{\mathbf{G}}|}{2K_z} \quad \text{and} \quad \gamma^{(1)} - \gamma^{(2)} \equiv \frac{2\pi}{\xi_{\mathbf{G}}}, \quad (12)$$

where $\xi_{\mathbf{G}}$ is an extinction distance [14]. For a centrosymmetric crystal $\phi_{\mathbf{G}} = 0$ and $U_{-\mathbf{G}} = U_{\mathbf{G}}$.

Using relations Eqs. (10) and (12), one obtains from Eq. (2)

$$C_{\mathbf{0}}(z) = \cos\frac{\pi z}{\xi_{\mathbf{G}}} \quad \text{and} \quad C_{\mathbf{G}}(z) = ie^{i\phi_{\mathbf{G}}} \sin\frac{\pi z}{\xi_{\mathbf{G}}} \quad (13)$$

and for an optimization criterion from Eq. (8)

$$\sum_{\mathbf{a}} \text{Im}\left[e^{-i\mathbf{G}\cdot\mathbf{a}}(-i)e^{-i\phi_{\mathbf{G}}} \sin\frac{\pi a_z}{\xi_{\mathbf{G}}} \cos\frac{\pi a_z}{\xi_{\mathbf{G}}}\right] = -\sum_{\mathbf{a}} \text{Im}[ie^{-i(\mathbf{G}\cdot\mathbf{a}+\phi_{\mathbf{G}})}]\frac{1}{2}\sin\frac{2\pi a_z}{\xi_{\mathbf{G}}} = -\frac{1}{2}\sum_{\mathbf{a}} \sin\frac{2\pi a_z}{\xi_{\mathbf{G}}} \cos(\mathbf{G}\cdot\mathbf{a} + \phi_{\mathbf{G}}). \quad (14)$$

By writing $\mathbf{a} = \mathbf{R} + \mathbf{u}$, where $\mathbf{R}$ is a lattice vector and $\mathbf{u}$ is a basis vector, and by neglecting $u_z/\xi_{\mathbf{G}}$ in the argument of sinus, we obtain

$$-\frac{1}{2}\sum_{\mathbf{R}} \sin\frac{2\pi R_z}{\xi_{\mathbf{G}}} \sum_{\mathbf{u}} \cos(\mathbf{G}\cdot\mathbf{u} + \phi_{\mathbf{G}}), \quad (15)$$

where we used that $e^{i\mathbf{G}\cdot\mathbf{R}} = 1$ for all reciprocal-lattice vectors **G** and lattice vectors **R**.

We introduce the *thickness function* by

$$\frac{1}{N_{xy}}\sum_{\mathbf{R}} \sin\frac{2\pi R_z}{\xi_{\mathbf{G}}} = \frac{\cos\frac{\pi c}{\xi_{\mathbf{G}}} - \cos\left(\frac{2\pi t}{\xi_{\mathbf{G}}} - \frac{\pi c}{\xi_{\mathbf{G}}}\right)}{2\sin\frac{\pi c}{\xi_{\mathbf{G}}}} \approx \frac{\xi_{\mathbf{G}}}{\pi c}\sin^2\frac{\pi t}{\xi_{\mathbf{G}}}, \quad (16)$$

where N_{xy} is the number of illuminated unit cells in the xy plane, c is the lattice parameter, t is the thickness of the crystal, and N_z is the number of cells in the z direction, so that $t = N_z c$. The approximation is valid when $\pi c \ll \xi_{\mathbf{G}}$.

Thus, to maximize the EMCD signal, we need to optimize the thickness function [Eq. (16)] and an expression reminding of a structure factor:

$$\sum_{\mathbf{u}} \cos(\mathbf{G}\cdot\mathbf{u} + \phi_{\mathbf{G}}) \equiv \text{Re}\left[e^{-i\phi_{\mathbf{G}}} \sum_{\mathbf{u}} e^{-i\mathbf{G}\cdot\mathbf{u}}\right], \quad (17)$$

where $\phi_{\mathbf{G}}$ is a phase of Fourier component of scattering potential $U_{\mathbf{G}}$, which includes contributions of *all atoms* within the unit cell, while the sum over basis vectors **u** runs only over atoms of the *species*, for which we want to measure the core-level excitation, e.g., only iron atoms in the FeGe crystal. In the following text, we refer to such an expression as a *partial structure factor*.

A practical optimization procedure would run over all **G** vectors with low Miller indices (otherwise it becomes cumbersome to set the two-beam orientation) searching for candidates that maximize Eq. (17). If the sample thickness is known, then one could simultaneously check for the value of the thickness function. Alternatively, an optimum thickness can be suggested for a given $\xi_{\mathbf{G}}$, specifically $t = \xi_{\mathbf{G}}/2$.

Importantly, the optimization procedure outlined above can be easily implemented in a computer program, which would perform all these optimizations within fractions of a second for an arbitrary crystal structure provided by a user. Such

software is expected to make EMCD experiments easier for a wider range of experimentalists interested in employing this method of magnetic measurement. An optional final step could be an explicit inelastic scattering simulation of the energy-filtered diffraction pattern to aid selection of the optimal detector orientation and size. Actual implementation of these procedures is in progress and will be reported elsewhere [15].

Note that a more careful optimization would require us to optimize the signal-to-noise ratio (SNR), which also depends on the nonmagnetic components of the scattering cross section and power-law background signal.

A careful reader could point out that there are many more maxima of the thickness function, Eq. (16), specifically at thicknesses $t = (2n+1)\xi_{\mathbf{G}}/2$, where n is a non-negative integer. However, they are not favorable for the following reason: the nonmagnetic component of the inelastic scattering monotonously increases with the sample thickness, while the magnetic one oscillates with thickness. If we assume a simple linear increase of the nonmagnetic component with thickness, then the relative strength of the EMCD signal at the maxima of the thickness function decreases proportionally to $1/(2n+1)$. It can be shown that the signal-to-noise ratio also drops, approximately proportionally to $1/\sqrt{2n+1}$. We should also note that here we have completely neglected absorption effects, which would further complicate the situation for thicker crystals.

III. SIMULATIONS

As an example system for application of this procedure we chose an FeGe crystal in the B20 phase; see Fig. 1(a). The helimagnet FeGe, which exhibits a complex Skyrmionic spin texture [16], can be easily magnetically saturated by the field in the microscope objective lens at low temperatures [17]. In fact, this system served as an initial motivation for this work. Repeated EMCD experiments with this material, which preceded the theoretical results presented here, have failed to detect any EMCD signal in a three-beam orientation with $\mathbf{G} = (200)$, following the otherwise standard "recipe" of the double-difference procedure [7].

In a three-beam orientation there are three pairs of beams, which can contribute to the EMCD: (1) $[\mathbf{0}, \mathbf{G}]$, (2) $[\mathbf{0}, -\mathbf{G}]$, and (3) $[\mathbf{G}, -\mathbf{G}]$; see Fig. 1(b). A general analytical treatment for noncentrosymmetric materials, such as FeGe, is cumbersome and will not be attempted here. In Appendix B we deal with a centrosymmetric three-beam orientation, or with a situation with real-valued $U_{\mathbf{G}}$, which is applicable here since $U_{(200)}$ is real. Qualitatively, these three pairs lead to three groups of terms in the inelastic scattering cross-section, each with its own *partial structure factor*. Two of them lead to a *partial structure factor* with $\mathbf{G} = \pm(200)$ and the last one to $\mathbf{G} = \pm(400)$. The $\pm\mathbf{G} = (200)$ beams have equal phases (see Appendix B), while the *partial structure factor* is real (Table I), therefore according to Eq. (8) mutual interference of this pair of beams doesn't contribute to the EMCD signal. What remains are the two pairs of the terms with $\mathbf{G} = \pm(200)$. Both structure factors are real and therefore equal. At first sight there seems to be no reason for not detecting a typical three-beam orientation type of EMCD distribution. So where is the problem with this system?

TABLE I. List of $\mathbf{G}$ vectors treated in this paper, together with those with $h, k, l < 5$ having real part of their *partial structure factor* [PSF; Eq. (17)] larger than 2.5.

$\mathbf{G}$	$\phi_{\mathbf{G}}$	$\xi_{\mathbf{G}}$	PSF
{2, 0, 0}	π	222 nm	0.501
{4, 0, 0}	π	144 nm	3.87
{2, 1, 0}	$\pi/2 \pm \pi/2$	87 nm	2.98
{4, 4, 0}	0	263 nm	3.75
{2, 2, 2}	± 1.98	1180 nm	3.58
{4, 4, 4}	± 2.80	389 nm	3.40
{3, 2, 0}	$\pm\pi/2$	1550 nm	-3.28
{4, 2, 1}	$-1.45 \pm \pi/2$	222 nm	2.85
{4, 3, 2}	$-0.58 \pm \pi/2$	2710 nm	2.70
{2, 0, 1}	$\pm\pi/2$	1090 nm	2.62

The issue is with the value of the *partial structure factor*. For $\mathbf{G} = \pm(200)$ the $\sum_{\mathbf{u}} \cos(\mathbf{G}\cdot\mathbf{u} + \phi_{\mathbf{G}}) = 0.501$. In its amplitude, this is approximately $\frac{1}{8}$th of the maximal value of 4—as there are four Fe atoms in the unit cell of FeGe. This suppresses the cross terms of the $\mathbf{0}$ beam with $\pm\mathbf{G}$ beams almost by an order of magnitude. Because this interference is the primary source of expected EMCD, the attainable EMCD signal strength is going to be on the order of 1% or below, therefore most likely buried under the noise level. This is confirmed by an explicit simulation [10] shown in Fig. 2(a), where across all thicknesses the relative strength of EMCD is very low, except for thin vertical stripes covering a very small fraction of a diffraction plane; see Fig. 1(b).

Simulations were performed using the MATS.V2 algorithm [10] with a summation cutoff of 10^{-5}. The incoming beam, a plane wave, was tilted approximately 10° from the [001] zone axis. Weickenmeier-Kohl scattering potentials [18] were used and the absorptive potential was modelled as $U'_{\mathbf{G}} = 0.1iU_{\mathbf{G}}$. In Fig. 2 we show the thickness dependence of the $\sigma_{\pm\pm}(E)$ integrated over the energy-loss range covering the L_3 edge of iron. The same detector orientation and collection angles were assumed as in the experiment shown below; see insets in Fig. 3.

Now that we have demonstrated the importance of the *partial structure factor*, we will apply the optimization procedure outlined in the previous section. Limiting ourselves to the $\mathbf{G}$ vectors with h, k, l indices with absolute value smaller than 5, Table I lists the $\mathbf{G}$ vectors leading to the largest real parts of the *partial structure factor*. This list suggests that an exact two-beam orientation with $\mathbf{G} = (400)$ [see Fig. 1(c)] should be a much better experimental geometry, offering a more than 7× larger *partial structure factor* multiplying the imaginary part of MDFF. Note that a three-beam orientation with $\mathbf{G} = (400)$ would be the same as a three-beam case with $\mathbf{G} = (200)$. With (200) being closer to (000), these diffraction spots would be always present in a three-beam orientation with $\mathbf{G} = (400)$. That is why it is necessary to turn to a two-beam case. To probe this qualitative suggestion, we have performed a simulation and the results are shown in Fig. 2(b). A striking difference is immediately obvious—in the range of

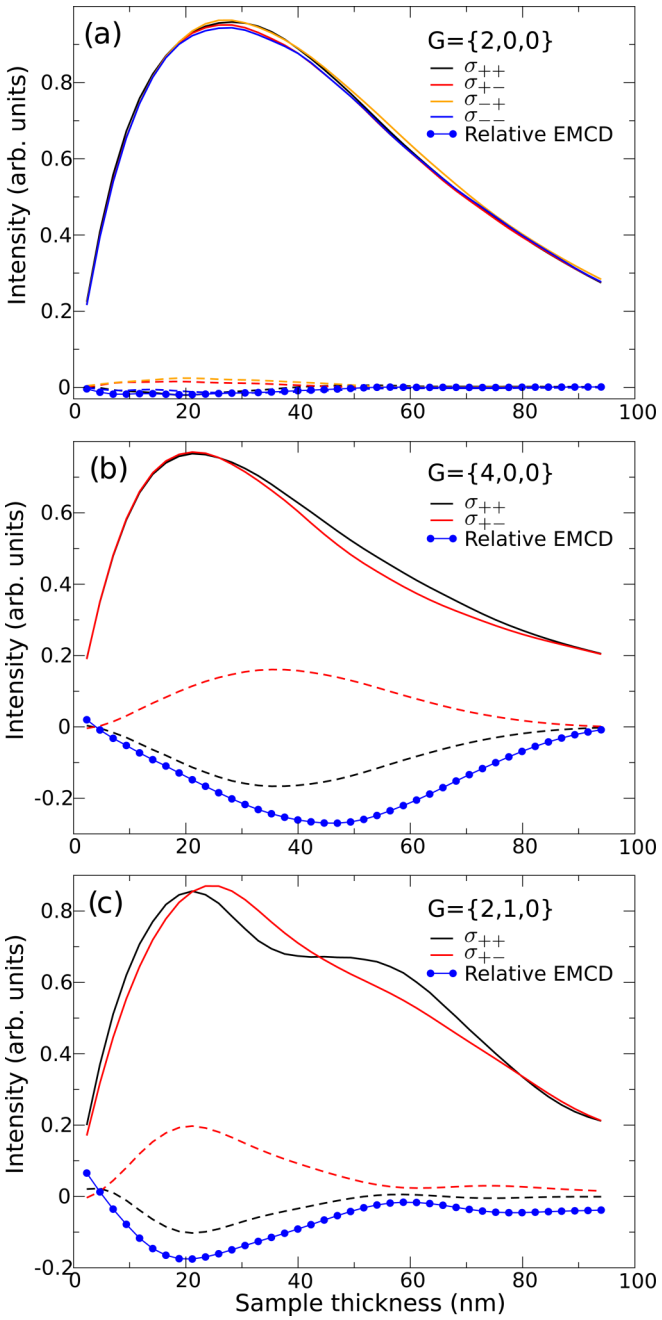

FIG. 2. Simulations of nonmagnetic (solid lines) and EMCD (dashed lines) components of the scattering cross section for Fe L_3 edge in FeGe crystal. Acceleration voltage was set to 300 kV and orientations was (a) three-beam orientation with $\mathbf{G} = \{2, 0, 0\}$, (b) two-beam orientation with $\mathbf{G} = \{4, 0, 0\}$, and (c) two-beam orientation with $\mathbf{G} = \{2, 1, 0\}$.

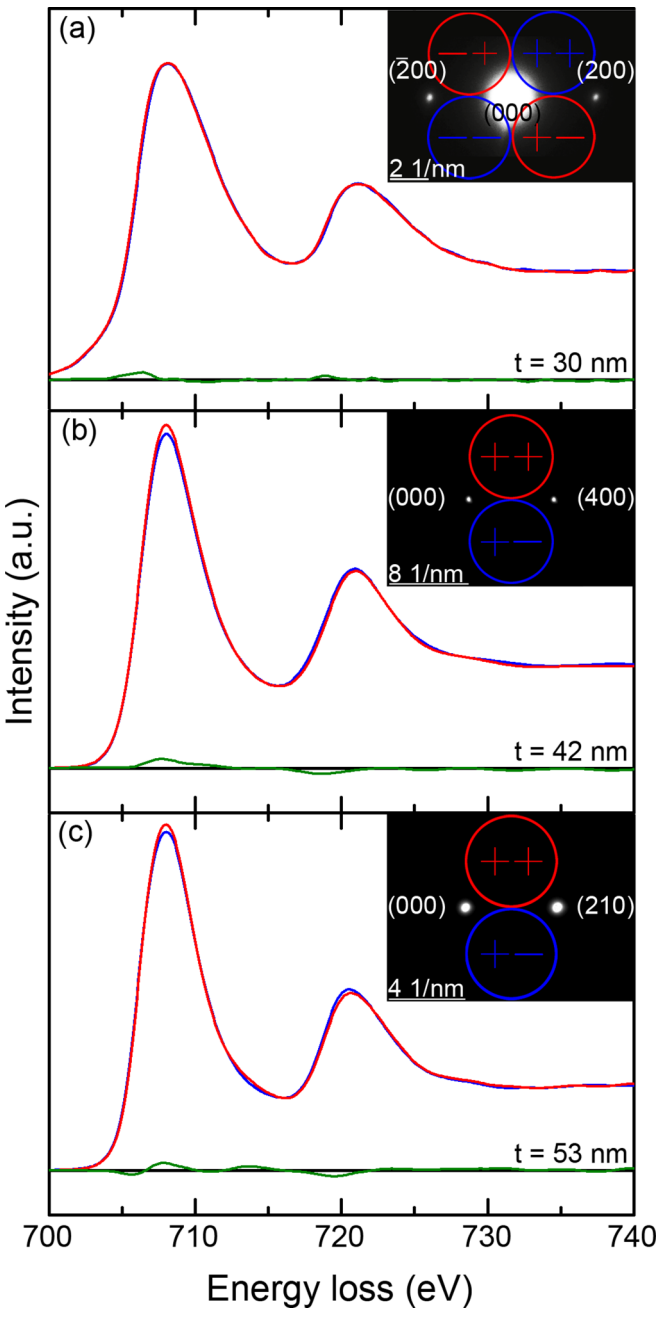

FIG. 3. EEL spectra measured in two- and three-beam conditions with their respective EMCD signal (difference) in green. The aperture positions corresponding to the spectra are displayed as inset. Measurements in the two-beam case show a dichroic signal (b) and (c), whereas the asymmetry at the absorption edges disappears when spectra are measured in the three-beam case (a). Furthermore the thickness of the respective investigated sample areas is denoted in the panels.

sample thicknesses between 20 and 60 nm there is a sizable EMCD signal spread over a large part of the diffraction plane; see Fig. 1(c). For larger thicknesses it decreases in agreement with the thickness function, Eq. (16), which has a period equal to the extinction distance of 144 nm. Thus a simulation, which considers hundreds of beams and full double channeling, confirms the simple qualitative prediction based on two-beam approximation and on values of *partial structure factor* and an extinction distance.

Inspecting Table I, another interesting suggestion is a two-beam orientation with $\mathbf{G} = (210)$. Although it has a somewhat decreased *partial structure factor* of 2.98, it has lower Miller indices and that should be helpful in setting the experimental crystal orientation. It also has rather low extinction distance,

so it should be suitable for thinner FeGe samples. And explicit simulation is shown in Fig. 2(c), which confirms a sizable EMCD with a maximum near a thickness of 20 nm. In this orientation EMCD is weaker than for $\mathbf{G} = (400)$, but still significantly higher than in a three-beam orientation with $\mathbf{G} = (200)$.

Interesting questions arise when considering the consequences of a large imaginary part of the *partial structure factor* for this system. The derivation given above for an exact two-beam orientation suggests that this doesn't bring any advantages. However, if we deviate slightly from the exact two-beam orientation (i.e., there will be nonzero excitation error $s_{\mathbf{G}}$), new terms appear and modify the picture. In Appendix A we generalize the derivation from Sec. II for a general two-beam approximation allowing for a tilt from exact two-beam orientation. Results shown there suggest that an imaginary *partial structure factor* should provide a stable nonzero EMCD at large thicknesses, being largest when dimensionless parameter w, characterizing the tilt away from exact two-beam orientation (see Appendix A), is equal to ± 1. The EMCD term acquires a prefactor of $\frac{w}{1+w^2} = \pm\frac{1}{2}$ that reduces its magnitude, nevertheless, once $t \gg \xi_{\mathbf{G}}$, the relative strength of EMCD should be only weakly dependent on sample thickness.

IV. EXPERIMENTS

To verify the above developed theory, EMCD experiments were performed in three different scattering geometries on a FeGe sample. Cf. Table I: the **G** vectors {4, 0, 0} and {2, 1, 0} are chosen, due to their real part *partial structure factors* and their accessibility in the setup of a two-beam case in the experiment. Additionally a three-beam orientation with $\mathbf{G} = (200)$, as already mentioned in Sec. III, was probed.

FeGe single crystals with the cubic B20 structure were grown via chemical vapor transport (CVT) in quartz tubes using an iodine transport agent. The crystal growth zone of the CVT reaction was kept at a temperature of 500 °C while the source zone was kept at a temperature of 560 °C [19,20]. After careful determination of the orientation using x-ray diffraction and electron backscatter diffraction, the crystal is embedded into a resin. Subsequently the embedded crystal is mechanically thinned in the direction of the [001] crystallographic axis to approximately 30 μm. Afterwards the sample is subjected to grazing incidence Ar^+ ion milling until holes form.

The EMCD experiments are performed in a double corrected FEI Titan^3 80–300 microscope operated at an acceleration voltage of 300 kV. All measurements were conducted at a sample temperature of 90 K using a Gatan double tilt liquid-nitrogen cooling holder. With the objective lens of the microscope fully excited, the sample is exposed to a 2.2 T magnetic field parallel to the optical axis of the microscope. In these conditions the cubic FeGe is in the so-called *field polarized* phase with all the spins aligned parallel to the applied external field [17], yielding the maximal dichroic signal. To prepare the respective two- and three-beam orientations the α and β tilt of the sample holder is used to tilt the sample with respect to the electron beam, until the desired conditions in the diffraction patterns (see Fig. 3 insets) are reached. The camera length with respect to the 1 mm entrance aperture of the Gatan Tridiem 865 energy filter is adjusted in such a way that the probed areas in the diffraction patterns are maximal (see colored circles in the diffraction patterns in the insets of Fig. 3). From each of these positions 100 electron energy-loss (EEL) spectra are recorded, with a single spectrum acquisition time of 0.5 s and a dispersion 0.5 eV per pixel, containing the Fe L_3 and L_2 edges. Afterwards spectra from each aperture position are resampled by a factor of 4 on the energy scale, aligned with respect to the Fe L_3 edge and summed. Subsequently the backgrounds of these sum spectra are removed. In order to account for multiple scattering, these spectra are deconvoluted with their respective low-loss spectra using the Richardson-Lucy algorithm [21,22] (15 iterations). Furthermore the low-loss spectra are used to determine the thicknesses of the investigated sample areas, denoted in the respective panels in Fig. 3.

For the two-beam cases [Figs. 3(b) and 3(c)] the treated spectra from aperture positions "++" and "+–" are postedge normalized and subtracted, resulting in the EMCD signal (green curves). For **G** vectors {4, 0, 0} and {2, 1, 0} a clear asymmetry at the Fe L_3 edge, which reverses sign at the Fe L_2 edge, is visible. This is also reflected in the EMCD signal which is only nonzero at the positions of the edges. In the case of the three-beam condition the spectra from all four aperture positions are postedge normalized and the spectra $\sigma_{++}(E), \sigma_{--}(E)$ and $\sigma_{+-}(E), \sigma_{-+}(E)$ are summed respectively, displayed in Fig. 3(a). The double difference procedure leads to the dichroic signal denoted as a green curve. In contrast to the two-beam cases no asymmetry at the absorption edges is visible, verifying the importance of the *partial structure factor* in EMCD experiments. Nevertheless it also has to be noted that although an EMCD signal is qualitatively visible in the two-beam conditions, the signal-to-noise ratio is still too low to reproducibly get quantitative results for the ratio of orbital to spin magnetic moment from the dichroic signal.

V. DISCUSSION

The close connection of the *partial structure factor* and the position of the magnetic atoms within the crystal becomes particular obvious, when comparing the two- and three-beam condition for the FeGe case in Fig. 1. In Fig. 1(a) the blue sheets indicate the {2, 0, 0} and {4, 0, 0} lattice planes, which intersect all magnetic Fe atoms in the unit cell. For the three-beam case in Fig. 1(b) electrons are only scattered at a fraction of these planes, whereas for the two-beam case in Fig. 1(c) planes contributing to the scattering contain all magnetic atoms of the unit cell. This quite simplistic picture nevertheless allows for allocating a meaning to the *partial structure factor* in real space.

So far the optimization of the EMCD signal is only discussed for ferromagnets. For more complex magnetic structures like ferrimagnets the *partial structure factor* can contain terms with positive and negative sign influencing the total sum in Eq. (17). Eventually these terms can be also weighted by (different) sizes of magnetic moments to include the different sublattices. Moreover the *partial structure factor* can be further generalized to study complex noncollinear magnetic structures, allowing for relatively fast simulation of an EMCD

signal of intrinsic or larger scale structures like skyrmions or domain walls to set the right experimental conditions.

Turning the argument around for magnets with several nonequivalent magnetic atoms of the same species, the *partial structure factor* can also be used to separate these structures. The task would be then to find a $\mathbf{G}_1$, which minimizes the signal from sublattice "2" and maximizes the signal from sublattice "1," and another $\mathbf{G}_2$ for the opposite situation.

From an experimental point of view the quality of the respective two-beam orientation can only be checked by the intensity of the diffraction spots. However an exact two-beam orientation does not necessarily mean that $\mathbf{0}$ and $\mathbf{G}$ have equal intensity, since the Pendellösung modifies these intensities as a function of thickness. To account for this problem one possible solution could be to simulate the elastic diffraction pattern for the respective thickness to have a rough estimate for the intensity distribution in the experiment. In principle the experimental diffraction pattern could also be used as an input to a computer-controlled tilting system in the microscope to find the desired orientation.

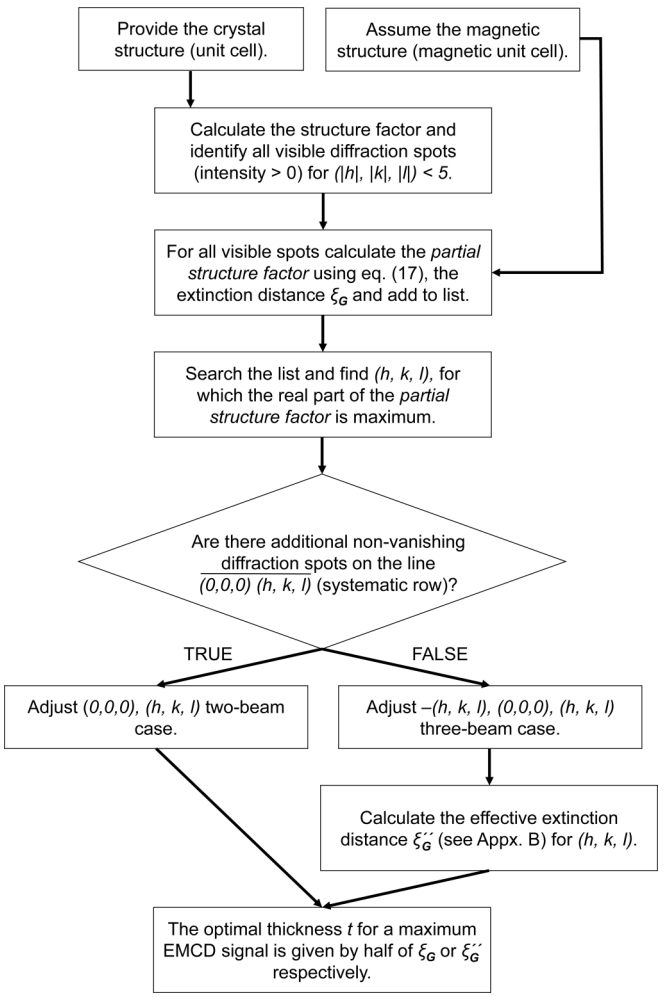

FIG. 4. Flowchart describing the guideline how to perform an EMCD experiment on an arbitrary crystal structure to get a maximum dichroic signal.

VI. CONCLUSIONS

In conclusion, we explicitly revised the theory of EMCD in a two-beam orientation. The introduced *partial structure factor* is identified as a parameter that can be optimized relatively easily in order to maximize the EMCD signal in the experiment by choosing the right crystal orientation. We have also discussed the effect of the thickness function on the strength of the dichroic signal. Furthermore the *partial structure factor* is calculated for several two-beam conditions and the three-beam orientation with $\mathbf{G} = (200)$ of the helimagnet FeGe in the B20 phase to get qualitative suggestions for which orientation is most suitable experimentally. The *partial structure factor* for the three-beam case is significantly decreased in comparison with the two-beam orientations. Additional simulations of the lateral distribution of the EMCD signal in the diffraction plane as a function of sample thickness confirm these findings. With the determined optimal experimental parameters EMCD signals of an actual fully saturated FeGe sample in two- and three-beam conditions are measured. As suggested by our developed theory a significant dichroic signal is detectable for the two-beam orientations, whereas it is absent in the three-beam case. In summary, our findings reveal the importance of the crystal orientation for EMCD measurements. Besides we provide an easy hands on tool for experimentalists to choose the optimal setup for their dichroic measurements. The general workflow of this optimization procedure for EMCD experiments on an arbitrary crystal structure is summarized in Fig. 4.

ACKNOWLEDGMENTS

We thank U. Nitzsche for technical assistance and H. Ali for helpful discussions. The authors are indebted to A. Pöhl for the preparation of the TEM sample. D.S.N. and J.R. acknowledge funding from the Swedish Research Council, the Göran Gustafsson Foundation, and the Carl Tryggers Foundation. Calculations were performed using resources of the Swedish National Infrastructure for Computing at the NSC Center.

APPENDIX A: GENERAL TWO-BEAM APPROXIMATION

In a two-beam approximation with a nonzero excitation error $s_{\mathbf{G}}$, the secular equation is

$$\begin{pmatrix} -2K_z\gamma & U_{-\mathbf{G}} \\ U_{\mathbf{G}} & -2K_z\gamma - G^2 - 2\mathbf{K}\cdot\mathbf{G} \end{pmatrix}\begin{pmatrix} C_{\mathbf{0}} \\ C_{\mathbf{G}} \end{pmatrix} = 0 \quad \text{(A1)}$$

and solving it gives for elongations

$$\gamma^{(1,2)} = \frac{-(G^2 + 2\mathbf{K}\cdot\mathbf{G}) \pm \sqrt{(G^2 + 2\mathbf{K}\cdot\mathbf{G})^2 + 4|U_{\mathbf{G}}|^2}}{4K_z} \quad \text{(A2)}$$

and the relation between Bloch coefficients is

$$C_{\mathbf{G}}^{(1,2)} = e^{i\phi_{\mathbf{G}}} C_{\mathbf{0}}^{(1,2)} \frac{2K_z\gamma^{(1,2)}}{|U_{\mathbf{G}}|}. \quad \text{(A3)}$$

More commonly, the elongations are written in terms of dimensionless parameter $w = -\frac{G^2+2\mathbf{K}\cdot\mathbf{G}}{2|U_{\mathbf{G}}|}$ and extinction

distance $\xi_{\mathbf{G}}$ [see Eq. (12)] as

$$\gamma^{(1,2)} = \frac{1}{2\xi_{\mathbf{G}}}[w \pm \sqrt{1+w^2}]. \tag{A4}$$

The *effective* extinction distance $\xi'_{\mathbf{G}}$ is given by

$$\gamma^{(1)} - \gamma^{(2)} = \frac{\sqrt{1+w^2}}{\xi_{\mathbf{G}}} \equiv \frac{1}{\xi'_{\mathbf{G}}} \tag{A5}$$

and for z-dependent Bloch coefficients from Eq. (2) we obtain

$$C_{\mathbf{0}}(z)e^{-i\pi wz/\xi_{\mathbf{G}}} = \cos\frac{\pi z}{\xi'_{\mathbf{G}}} - \frac{iw}{\sqrt{1+w^2}}\sin\frac{\pi z}{\xi'_{\mathbf{G}}}, \tag{A6}$$

$$C_{\mathbf{G}}(z)e^{-i\pi wz/\xi_{\mathbf{G}}} = \frac{ie^{i\phi_{\mathbf{G}}}}{\sqrt{1+w^2}}\sin\frac{\pi z}{\xi'_{\mathbf{G}}}. \tag{A7}$$

In an exact two-beam orientation the term $G^2 + 2\mathbf{K}\cdot\mathbf{G} = 0$, or equivalently $w = 0$ and $\xi'_{\mathbf{G}} = \xi_{\mathbf{G}}$, and results from the main text are reobtained.

Following now the optimization criterion Eq. (8) leads to a more complicated expression,

$$-\sum_{\mathbf{a}} \mathrm{Im}\left\{e^{-i(\mathbf{G}\cdot\mathbf{a}+\phi_{\mathbf{G}})}\left[\frac{i}{2}\frac{\sin\frac{2\pi a_z}{\xi'_{\mathbf{G}}}}{\sqrt{1+w^2}} + \frac{w}{2}\frac{1-\cos\frac{2\pi a_z}{\xi'_{\mathbf{G}}}}{1+w^2}\right]\right\}. \tag{A8}$$

Splitting again the sum over $\mathbf{a} = \mathbf{R} + \mathbf{u}$ into two sums, neglecting $u_z/\xi'_{\mathbf{G}}$ in sines and cosines, one obtains two terms for optimization; first

$$-\frac{1}{2\sqrt{1+w^2}}\sum_{\mathbf{R}}\sin\frac{2\pi R_z}{\xi'_{\mathbf{G}}}\sum_{\mathbf{u}}\cos(\mathbf{G}\cdot\mathbf{u}+\phi_{\mathbf{G}}), \tag{A9}$$

which is an equivalent of what we have obtained above, and second

$$\frac{w}{2(1+w^2)}\sum_{\mathbf{R}}\left(1-\cos\frac{2\pi R_z}{\xi'_{\mathbf{G}}}\right)\sum_{\mathbf{u}}\sin(\mathbf{G}\cdot\mathbf{u}+\phi_{\mathbf{G}}), \tag{A10}$$

which brings some new aspects. First, it is proportional to the *imaginary* part of the partial structure factor. Second, and more surprising: every single unit cell of the system contributes with a non-negative prefactor, because the cosine in the sum over $\mathbf{R}$ cannot be larger than 1.

We can again evaluate the sum over $\mathbf{R}$. For the first term we obtain the same thickness function as in Eq. (16), and for the second term

$$\frac{1}{N_{xy}}\sum_{\mathbf{R}}\left(1-\cos\frac{2\pi R_z}{\xi'_{\mathbf{G}}}\right) = \frac{t}{c} - \frac{1}{2} - \frac{\sin\left(\frac{2\pi t}{\xi'_{\mathbf{G}}} - \frac{\pi c}{\xi'_{\mathbf{G}}}\right)}{2\sin\frac{\pi c}{\xi'_{\mathbf{G}}}} \approx \frac{t}{c} - \frac{\xi'_{\mathbf{G}}}{2\pi c}\sin\frac{2\pi t}{\xi'_{\mathbf{G}}}, \tag{A11}$$

which for small thicknesses ($t \ll \xi'_{\mathbf{G}}$) is close to zero, however for large thicknesses ($t \gg \xi'_{\mathbf{G}}$) the term t/c dominates. This leads to an interesting and unexpected suggestion: if the structure of the material allows us to choose a systematic row condition with the partial structure factor having a *large imaginary part*, then for thick crystals it should be advantageous to set the orientation such that we maximize the amplitude of the prefactor $\frac{w}{2(1+w^2)}$, which is $\pm\frac{1}{4}$ obtained for $w = \pm 1$, or in other words

$$G^2 + 2\mathbf{K}\cdot\mathbf{G} = \pm 2|U_{\mathbf{G}}|, \tag{A12}$$

and a sizable EMCD should be detectable at large thicknesses. One should however keep in mind that at large sample thicknesses this simple two-beam approximation might not be accurate.

APPENDIX B: THREE-BEAM ORIENTATION

In an exact three-beam orientation ($\mathbf{K}\cdot\mathbf{G} = 0$) the secular equation in the three-beam approximation becomes

$$\begin{pmatrix} -2K_z\gamma - G^2 & U_{-\mathbf{G}} & U_{-2\mathbf{G}} \\ U_{\mathbf{G}} & -2K_z\gamma & U_{-\mathbf{G}} \\ U_{2\mathbf{G}} & U-\mathbf{G} & -2K_z\gamma - G^2 \end{pmatrix}\begin{pmatrix} C_{-\mathbf{G}} \\ C_{\mathbf{0}} \\ C_{\mathbf{G}} \end{pmatrix} = 0. \tag{B1}$$

In noncentrosymmetric systems potentials $U_{\pm\mathbf{G}}$, $U_{\pm 2\mathbf{G}}$ can be complex. In such case the algebra becomes too cumbersome. However, in cases when the potentials are real—and for specific $\mathbf{G}$ that can happen also in a noncentrosymmetric case—then the analytical solution is tractable, as will be shown below.

There are three Bloch waves, which are solutions of this eigenproblem. One can exploit symmetries of the eigenproblem [23] to show that one of them, let's mark it Bloch-wave number 1, has $C^{(1)}_{\mathbf{0}} = 0$. Because $C_{\mathbf{0}}$ is also an excitation coefficient, we can neglect this Bloch wave, since it won't be excited when the plane wave enters the crystal. The other two Bloch waves have $C^{(2,3)}_{-\mathbf{G}} = C^{(2,3)}_{\mathbf{G}}$ and their *Anpassung* factors are

$$\begin{aligned}\gamma^{(2,3)} &= \frac{U_{2\mathbf{G}} - G^2 \pm \sqrt{(U_{2\mathbf{G}} - G^2)^2 + 8U^2_{\mathbf{G}}}}{4K_z} \\ &= \frac{1}{2}\left[s'_{\mathbf{G}} \pm \sqrt{s'^2_{\mathbf{G}} + \frac{2}{\xi^2_{\mathbf{G}}}}\right] \\ &= \frac{1}{2\xi_{\mathbf{G}}}[w' \pm \sqrt{2+w'^2}],\end{aligned} \tag{B2}$$

where we introduced *effective* excitation error $s'_{\mathbf{G}} = \frac{U_{2\mathbf{G}}-G^2}{2K_z}$, extinction distance as in the exact two-beam case $\xi_{\mathbf{G}} = \frac{K_z}{U_{\mathbf{G}}}$, and their product as a dimensionless parameter $w' = s'_{\mathbf{G}}\xi_{\mathbf{G}}$. We can then similarly as in the general two-beam approximation, introduce an effective extinction distance $\xi''_{\mathbf{G}} = \frac{\xi_{\mathbf{G}}}{\sqrt{2+w'^2}}$. It's almost the same as in the general two-beam approximation, Eq. (A5), just with redefined w' and a 2 instead of 1 in the square-root expression.

For the Bloch wave numbers 2 and 3 the relation between Bloch coefficients is $C^{(2,3)}_{\mathbf{G}} = C^{(2,3)}_{\mathbf{0}}\xi_{\mathbf{G}}\gamma^{(2,3)}$. Normalization of Bloch waves leads to a condition

$$\left|C^{(2,3)}_{\mathbf{0}}\right|^2 = \frac{1}{2}\left[1 \pm \frac{w'}{\sqrt{2+w'^2}}\right], \tag{B3}$$

which can be used to derive

$$C_{\mathbf{0}}(z) = e^{\frac{i\pi w' z}{\xi_{\mathbf{G}}}}\left[\cos\frac{\pi z}{\xi''_{\mathbf{G}}} - \frac{iw'}{\sqrt{2+w'^2}}\sin\frac{\pi z}{\xi''_{\mathbf{G}}}\right], \quad \text{(B4)}$$

$$C_{\pm\mathbf{G}}(z) = e^{\frac{i\pi w' z}{\xi_{\mathbf{G}}}}\frac{i}{\sqrt{2+w'^2}}\sin\frac{\pi z}{\xi''_{\mathbf{G}}}. \quad \text{(B5)}$$

Note the formal similarity with expressions in two-beam approximation, Eqs. (A6) and (A7).

In a centrosymmetric crystal structure the structure factor is real, thus the EMCD prefactor from Eq. (8) becomes

$$\sum_{\mathbf{a}}\cos(\mathbf{G}\cdot\mathbf{a})\mathrm{Im}[C_{\mathbf{0}}(a_z)C^{\star}_{\mathbf{G}}(a_z)] = -\frac{1}{2\sqrt{2+w'^2}}\sum_{\mathbf{u}}\cos(\mathbf{G}\cdot\mathbf{u})\sum_{\mathbf{R}}\sin\frac{2\pi R_z}{\xi''_{\mathbf{G}}}. \quad \text{(B6)}$$

Note that with real structure factor there is no cross term between $C_{\mathbf{G}}(z)$ and $C_{-\mathbf{G}}(z)$ that would contribute to the EMCD, since the product of $C_{\mathbf{G}}(z)C^{\star}_{-\mathbf{G}}(z)$ is real.

Another remark is related to w': while in two-beam approximation w was a parameter whose value could change as a function of tilt from the exact two-beam orientation, in this treatment of exact three-beam orientation it has a fixed value. Only in such conditions there is a tractable analytical treatment of three-beam approximation.

Returning to the case of FeGe from the main text, in three-beam orientation with $\mathbf{G} = (200)$, the potentials $U_{\pm\mathbf{G}}, U_{\pm\mathbf{2G}}$ are real. Therefore one can use the analytical treatment outlined in this appendix. The *partial* structure factor over iron atoms then has a value

$$\sum_{\mathbf{u}}\cos(\mathbf{G}\cdot\mathbf{u}) \approx 0.501, \quad \text{(B7)}$$

which is far from the optimized values in Table I, explaining the weak EMCD observed in this experimental geometry.

[1] P. Schattschneider, S. Rubino, C. Hébert, J. Rusz, J. Kuneš, P. Novák, E. Carlino, M. Fabrizioli, G. Panaccione, and G. Rossi, Nature (London) **441**, 486 (2006).

[2] J. C. Idrobo, J. Rusz, J. Spiegelberg, M. A. McGuire, C. T. Symons, R. Raju Vatsavai, C. Cantoni, and A. R. Lupini, Adv. Chem. Struct. Imaging **2**, 5 (2016).

[3] J. Rusz, S. Muto, J. Spiegelberg, R. Adam, K. Tatsumi, D. E. Bürgler, P. M. Oppeneer, and C. M. Schneider, Nat. Commun. **7**, 12672 (2016).

[4] T. Thersleff, J. Rusz, B. Hjörvarsson, and K. Leifer, Phys. Rev. B **94**, 134430 (2016).

[5] C. Hébert and P. Schattschneider, Ultramicroscopy **96**, 463 (2003).

[6] P. Schattschneider, M. Stöger-Pollach, S. Rubino, M. Sperl, Ch. Hurm, J. Zweck, and J. Rusz, Phys. Rev. B **78**, 104413 (2008).

[7] H. Lidbaum, J. Rusz, A. Liebig, B. Hjörvarsson, P. M. Oppeneer, E. Coronel, O. Eriksson, and K. Leifer, Phys. Rev. Lett. **102**, 037201 (2009).

[8] S. Schneider, D. Pohl, S. Löffler, J. Rusz, D. Kasinathan, P. Schattschneider, L. Schultz, and B. Rellinghaus, Ultramicroscopy **171**, 186 (2016).

[9] J. Rusz, S. Rubino, and P. Schattschneider, Phys. Rev. B **75**, 214425 (2007).

[10] J. Rusz, Ultramicroscopy **177**, 20 (2017).

[11] S. Löffler and W. Hetaba, Microscopy **67**, i60 (2018).

[12] H. Kohl and H. Rose, Adv. Electron. Electron Phys. **65**, 173 (1985).

[13] L. Reimer and H. Kohl, *Transmission Electron Microscopy - Physics of Image Formation* (Springer, New York, 2008).

[14] D. B. Williams and C. B. Carter, *Transmission Electron Microscopy - A Textbook for Materials Science* (Springer, New York, 2009).

[15] D. Negi and J. Rusz (unpublished).

[16] S. Schneider, D. Wolf, M. J. Stolt, S. Jin, D. Pohl, B. Rellinghaus, M. Schmidt, B. Büchner, S. T. B. Goennenwein, K. Nielsch, and A. Lubk, Phys. Rev. Lett. **120**, 217201 (2018).

[17] L. Lundgren, K. Å. Blom, and O. Beckman, Phys. Lett. A **28**, 175 (1968).

[18] A. Weickenmeier and H. Kohl, Acta Crystallogr., Sect. A: Found. Crystallogr. **47**, 590 (1991).

[19] M. J. Stolt *et al.*, Chem. Mater. **30**, 1146 (2018).

[20] M. Richardson, Acta Chem. Scand. **21**, 2305 (1967).

[21] W. H. Richardson, J. Opt. Soc. Am. **62**, 55 (1972).

[22] L. B. Lucy, Astron. J. **79**, 745 (1974).

[23] L. J. Allen and C. J. Rossouw, Ultramicroscopy **48**, 341 (1993).